A. Ishmurzin, M. Gruber-Pretzler, F. Mayer, M. Wu, A. Ludwig
Christian Doppler Laboratory for Multiphase Modeling of Metallurgical Processes,
Department of Metallurgy, University of Leoben, Leoben, Austria

Multiphase/multicomponent modeling of solidification processes: coupling solidification kinetics with thermodynamics

This paper is an extension and improvement of the previous work of the authors. It presents further development of a coupling method between a multiphase Eulerian solidification model and the thermodynamics of multicomponental alloys. The transport equations of the multiphase solidification model are closed by the interphase transfer/exchange terms. The derivation of these terms is based on the diffusion-controlled solidification kinetics and thermodynamics. Direct online coupling of a computational fluid dynamics solver with a thermodynamic software package is time-consuming, therefore a way to access thermodynamic data by means of the tabulation and interpolation technique (In-Situ Adaptive Tabulation) is suggested. The coupling procedure is described and tested with a 0-D solidification benchmark case. Additionally, the suggested coupling method is used to simulate a casting process of a CuSn6P0.5 round strand, which demonstrated the application potential of the coupling idea. The predicted macrosegregations of Sn and P for this casting process shows the same distribution pattern as observed in practice, namely positive segregation in the vicinity of the wall region and negative one in the center of the casting.

Keywords: Thermodynamics; Ternary; Solidification; Macrosegregation

1. Introduction

In order to model the solidification process, it is necessary to consider the conservation equations of mass, enthalpy and solute on the macroscopic scale, and the thermodynamic equilibrium of the multicomponent alloy system on the liquid–solid interfacial microscale. The actual solidification path of a multicomponent alloy is an important factor when describing solidification. It is governed by thermodynamics and, in addition, strongly influenced by kinetic effects such as cooling history and macroscopic transport phenomena.

During the last decade, multiphase models for solidification based on the volume averaging approach, which considers the different phases (liquid, solidified equiaxed and/or columnar phases) as spatially coupled and interpenetrating continua, [1–8] have been developed. Macroscopic conservation equations of mass, momentum, species and enthalpy are solved for all involved phases. Conservation equations are closed by supplemental closure laws like mass and species exchange at the liquid–solid interface due to solidification. Therefore, access to the thermodynamic data during solidification simulation is required. Most of the previous work was done for binary systems. A few trials were performed on multicomponent systems using simplified thermodynamics and also online coupling with thermodynamic software, although not for the Eulerian multiphase solidification model [9]. Linearized phase diagrams with constant liquidus slope and constant partitioning coefficients are usually used [10, 11].

At the same time great progress has been achieved in the field of computational thermodynamics [12, 13]. Using the so-called CALPHAD method, it is possible to predict phase evolutions and solidification paths taking into account effects of cooling rate, back diffusion, and coarsening [14–16]. Those methods, however, are limited to cases of small specimens solidifying under given conditions. Combeau and co-workers proposed a micro–macro segregation model [17–19], in which an 'open specimen', corresponding to the volume element in a larger system, was considered. The overall solute in the volume element is allowed to exchange with the neighboring elements. Hence, the access to thermodynamic data is given through the so-called mapping files.

The authors recently proposed a new method [20, 21] to couple the thermodynamic data with the multiphase solidification model, which is described later. The current paper is an extension and improvement of that previous work. Two critical points when coupling the solidification kinetics with thermodynamics in the multiphase solidification model are addressed in the present paper: i) derivation of closure laws for the solidification rate and the species partitioning at the liquid–solid interface and ii) a way to access thermodynamic data provided by thermodynamic software (for example Thermo-Calc) through the tabulation and interpolation technique ISAT (In-Situ Adaptive Tabulation) [22].

2. Model description

The multiphase solidification model with melt convection and grain sedimentation was described in [5–7]. The current paper focuses on the coupling between solidification kinetics and thermodynamics. Therefore, the model in this section is based on a simplified 0-D (only time dependence is considered) description where the melt flow and solid movement are not explicitly described. This kind of simplification allows us to concentrate on the actual coupling, by-

passing the details of the solidification model that take flow into account. On the other hand, thermodynamics is taken into account without any simplifications. The implementation of the proposed coupling for a multi-dimensional solidification model with melt convection and solid movement is straightforward [20–21].

The assumptions of the 0-D model are:

- there are only two phases involved during solidification, the liquid phase l and the solid columnar phase c,
- the morphology of the columnar trunks is cylindrical,
- the growth of the columnar trunk is controlled by diffusion,
- solidification occurs in an isolated volume element,
- local thermal equilibrium at the liquid–solid interface is assumed,
- solute partitioning occurs at the liquid–solid interface,
- the equilibrium concentrations of alloying elements in liquid and solid phase at the liquid–solid interface are different from the bulk concentrations, and
- species transport by back diffusion in the solid phase is ignored.

2.1. Conservation equations

Taking into account the aforementioned model assumptions, the conservation equations were as follows.
Mass conservation equations are:

$$\frac{df_c}{dt} = \frac{1}{\rho_c} M_{lc} \tag{1}$$

$$\frac{df_l}{dt} = -\frac{1}{\rho_l} M_{lc} \tag{2}$$

where f_l, f_c are volume fractions ($f_c + f_l = 1$), ρ_l, ρ_c are the densities of the phases, and M_{lc} is the mass transfer rate from liquid to solid due to solidification.

The species conservation equations are:

$$\frac{d}{dt}(f_c c_c^i) = \frac{1}{\rho_c} C_{lc}^i \tag{3}$$

$$\frac{d}{dt}(f_l c_l^i) = -\frac{1}{\rho_l} C_{lc}^i \tag{4}$$

where c_c^i is the mass fraction of the ith solute component in the solid phase, and c_l^i in the liquid phase. C_{lc}^i is the species exchange rate due to solidification:

$$C_{lc}^i = \tilde{c}_c^i M_{lc} \tag{5}$$

where $\tilde{c}_c^i$ is the equilibrium mass fraction of ith solute component of the solid phase, which applies at the liquid–solid interface.

Substituting (1) and (5) into (3), and substituting (2) and (5) into (4), we get

$$\frac{dc_c^i}{dt} = -\frac{M_{lc}}{\rho_c f_c}(c_c^i - \tilde{c}_c^i) \tag{6}$$

$$\frac{dc_l^i}{dt} = \frac{M_{lc}}{\rho_l f_l}(c_l^i - \tilde{c}_c^i) \tag{7}$$

Here, the equilibrium mass fraction $\tilde{c}_c^i$ is the thermodynamic quantity which must be determined from thermodynamics according to the local temperature.

2.2. Solidification kinetics

With the assumptions of diffusion controlled columnar growth, the growth velocity of the columnar phase v_c^i is calculated [21]

$$v_c^i = \frac{2D_l^i}{d_c} \frac{\tilde{c}_l^i - c_l^i}{\tilde{c}_l^i - \tilde{c}_c^i} \ln^{-1}\left(\frac{d_{max}}{d_c}\right) \tag{8}$$

Here, the D_l^i is the diffusion coefficient of the ith component in the liquid phase, d_c is the actual diameter of the columnar trunk, d_{max} is the maximum diameter of the columnar trunk, and $\tilde{c}_l^i$ is the equilibrium mass fraction of the ith solute component of the liquid phase, which applies at the liquid–solid interface. One can choose any arbitrary i^{th} component to determine the growth velocity, since the calculated v_c^i must fulfill the consistency relation

$$v_c^A \equiv v_c^B \equiv \cdots \equiv v_c^N \tag{9}$$

where N is the total number of solute components ($i = 1, \ldots, N$). As an example, let us consider a ternary system ($N = 2$). We use the indicies A and B to refer to the first and second alloying component of such a system. By applying Eq. (9), we get

$$D_l^A \frac{\tilde{c}_l^A - c_l^A}{\tilde{c}_l^A - \tilde{c}_c^A} = D_l^B \frac{\tilde{c}_l^B - c_l^B}{\tilde{c}_l^B - \tilde{c}_c^B} \tag{10}$$

Finally, the volume averaged mass transfer rate M_{lc}, used in the conservation equations (1), (2) and (6), (7), can be calculated as

$$M_{lc} = v_c^i S \rho_c A_r \tag{11}$$

where S is the total surface area of all growing columnar dendrites per unit volume, and A_r is the Avrami-factor responsible for taking the impingement during grain growth into account. It is derived in [26] and can be expressed as:

$$A_r = \begin{cases} 1, & d_c \leq \lambda_1 \\ f_l/f_{l,crit}, & d_c > \lambda_1 \end{cases} \tag{12}$$

where λ_1 is the primary dendrite spacing, and both the columnar diameter d_c and the the critical liquid volume fraction $f_{l,crit}$ are calculated assuming hexagonal arrangement of cylindrical trunks from geometrical considerations as follows. The columnar volume fraction is expressed as the ratio between the total volume and the volume of the columnar fraction:

$$f_c = \frac{\frac{3}{4}\pi d_c^2}{\frac{3\sqrt{3}}{2}\lambda_1^2} \tag{13}$$

from (13) the columnar diameter can be expressed as:

$$d_c = 2\sqrt{\frac{f_c \sqrt{3}}{2\pi}}\lambda_1 \tag{14}$$

Now the cylinders start to impinge when $d_c = \lambda_1$, and according to (14) the corresponding critical liquid fraction is:

$$f_{l,crit} = 1 - f_{c,crit} = 1 - \frac{\pi\sqrt{3}}{6} \qquad (15)$$

2.3. Thermodynamics

The approach presented is suitable for a thermodynamically consistent description of an alloying system with an arbitrary number of components. For simplicity reasons we will consider just a ternary system with two alloying components, denoted by A and B. The ternary phase diagram information of interest is provided by three functions that express two thermodynamic relations in the two-phase region where solidification takes place. The first thermodynamic relation is expressed via the function for the liquidus surface, which is defined by:

$$T_L = T_L(\tilde{c}_l^A, \tilde{c}_l^B) \qquad (16)$$

For a given temperature, as shown in Fig. 1, the equilibrium concentrations of the two components $\tilde{c}_l^A$ and $\tilde{c}_l^B$ belong to the same the liquidus line. Since local thermal equilibrium is assumed, the liquidus temperature T_L, which applies at the liquid–solid interface, is equal to the local volume average temperature T:

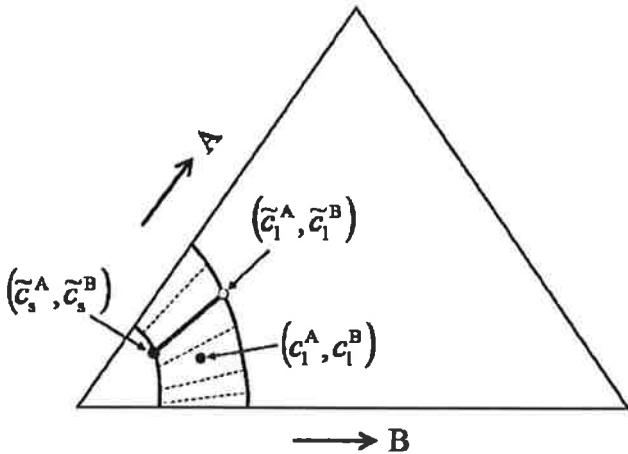$$T = T_L(\tilde{c}_l^A, \tilde{c}_l^B) \qquad (17)$$

Fig. 1. Schematic isothermal section of a ternary phase diagram for two alloying elements A and B. The given bulk composition (c_l^A, c_l^B), which lies in a two phase region, has a corresponding interfacial composition in the liquid $(\tilde{c}_l^A, \tilde{c}_l^B)$ that lies on the liquidus line. This point is in equilibrium with the solid interfacial composition $(\tilde{c}_s^A, \tilde{c}_s^B)$ in the solid. These equilibrium interfacial compositions are connected by a tie-line.

The second thermodynamic relation is the tie-line function, which describes the correspondence between solid and liquid composition of the alloying elements in equilibrium. Hence, the concentration of each alloying element in the solid phase is a function of liquid composition; it is expressed with the following two functions:

$$\tilde{c}_c^A = \tilde{c}_c^A(\tilde{c}_l^A, \tilde{c}_l^B) \qquad (18)$$

$$\tilde{c}_c^B = \tilde{c}_c^B(\tilde{c}_l^A, \tilde{c}_l^B) \qquad (19)$$

2.4. Coupling strategy

The strategy of coupling between solidification kinetics and thermodynamics is shown schematically in Fig. 2. The volume averaged quantities $(f_l, f_c, \bar{u}_l, T, c_l^A, c_l^B)$ are calculated by a CFD-solver based on the macroscopic conservation equations. In order to close the conservation equations, a volume averaged mass transfer rate M_{lc} is required. As expressed in Eqs. (8) and (11), M_{lc} is a function of thermodynamic equilibrium concentrations $(\tilde{c}_l^A, \tilde{c}_l^B, \tilde{c}_c^A, \tilde{c}_c^B)$, which are in turn determined according to the temperature T and the bulk concentrations c_l^A, c_l^B.

The system of multiphase flow equations is solved in an iterative way. The temperature T and the volume averaged concentrations of the melt c_l^A, c_l^B are taken from the last iteration of the CFD solver and are parameters in Eq. (10) and Eqs. (17)–(19). This system of four nonlinear algebraic equations is used to calculate the thermodynamic equilibrium concentrations $(\tilde{c}_l^A, \tilde{c}_l^B, \tilde{c}_c^A, \tilde{c}_c^B)$ which are required for closure of the macroscopic transport equation system by defining M_{lc}. If the thermodynamic relations (Eqs. (17)–(19)) could be expressed analytically, by for example using a local linearization approximation, it would be possible to solve the above 4 equations for 4 unknowns analytically. However, all industrial alloys exhibit nonlinear thermodynamics. Therefore, the solution of this equation system has to be carried out numerically.

In a general case the thermodynamic functions Eqs. (17)–(19) can be computed by calling thermodynamic software such as Thermo-Calc directly from a CFD-solver such as FLUENT. However, computational costs for calling and computing those functions are high because they have to be calculated for each volume element in each time step and each iteration. It has to be mentioned that the geometrical description of an industrial casting process may consist of thousands of such volume elements. In order to reduce computational costs, we suggest using an In-Situ Adaptive Tabulation (ISAT) approach [22], that stores computed values of
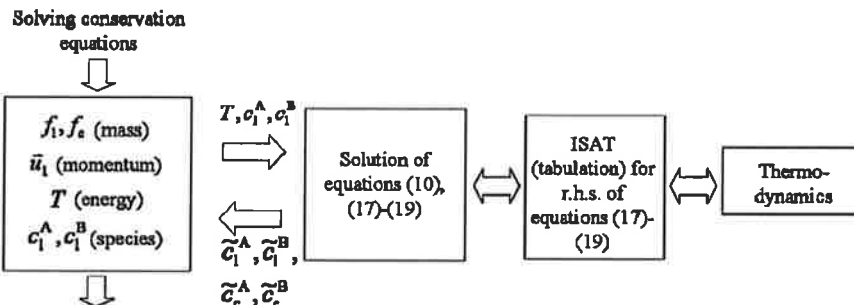

Fig. 2. Coupling strategy between solidification kinetics and thermodynamics.

thermodynamic functions in a table and looks them up when they are needed. Expensive calls to thermodynamic software are performed only for those function values which are not yet in the table.

3. Results and discussion

3.1. Verification of the model with 0-D solidification simulation

To verify the proposed model a 0-D solidification simulation of the CuSn6P0.5 alloy was performed. Equation (1) and the two equations Eq. (7) (for a ternary alloying system, $i = A, B$) define three equations that describe the 0-D solidification of a ternary alloy. In combination with appropriate initial conditions these three equations define an Initial Value Problem for an ordinary differential equation system. Temperature T is assumed to decrease linearly with time, starting from the initial temperature T_0 with a given constant cooling rate $\dot{T}_0$:

$$T(t) = T_0 - \dot{T}_0 t \tag{20}$$

This Initial Value Problem was integrated using the CFD-solver FLUENT with appropriate settings. The thermodynamic functions Eqs. (17)–(19) were interpolated based on tabulated Thermo-Calc data for the Cu−Sn−P system. Initial values were taken as follows: $f_c(0) = 10^{-5}$, for the columnar volume fraction and $c_l^{Sn}(0) = 0.06$ and $c_l^{P}(0) = 0.005$ for the mass fractions of Sn and P in the liquid phase. Inital temperature was set to $T_0 = 1297$ K and the cooling rate $\dot{T}_0 = 1$ K · s^{-1}. Figure 3 shows the Scheil-curves resulting from the ternary solidification simulation in comparison with appropriate Scheil-curves calculated with Thermo-Calc. Since the Thermo-Calc−Scheil model implies an infinite diffusion coefficient in the liquid but the proposed model uses a finite one, the diffusion coefficient for the 0-D model was increased to make comparison with Thermo-Calc results possible. Nevertheless minor differences are observed, as shown in the small windows in Fig. 3. Discrepancies also occur at high columnar volume fraction (B in Fig. 3). Here the presented model is not valid since it models only the formation of one solid phase from the liquid, whereas there are two solid phases forming directly from the liquid during the eutectic reaction. Apart from the differences mentioned, the curves produced by the proposed model are in good agreement with those calculated with Thermo-Calc.

Figure 4a−c shows the liquidus surface, $T = T_L(\tilde{c}_l^{Sn}, \tilde{c}_l^{P})$, and the solid concentration surfaces, $\tilde{c}_c^{Sn} = \tilde{c}_c^{Sn}(\tilde{c}_l^{Sn}, \tilde{c}_l^{P})$ and $\tilde{c}_c^{P} = \tilde{c}_c^{P}(\tilde{c}_l^{P}, \tilde{c}_l^{Sn})$, calculated and plotted in the Cu rich corner of the Cu−Sn−P system. Point A in the pictures gives the location of the initial alloy concentration of 0.06 mass fraction of Sn and 0.005 mass fraction of P whereas point B indicates the end of solidification.

Solidification of such bronze alloys starts with the formation of α dendrites according to thermodynamics as displayed in Fig. 4. The white/black dots in Fig. 4a−c show the solidification path calculated with the Thermo-Calc−Scheil model and the white/black line the solidification path according to the proposed model. As, during solidification, the first peritectic groove is crossed (P$_1$, Figs. 3 and 4), β phase is formed due to the peritectic reaction L + α → β.
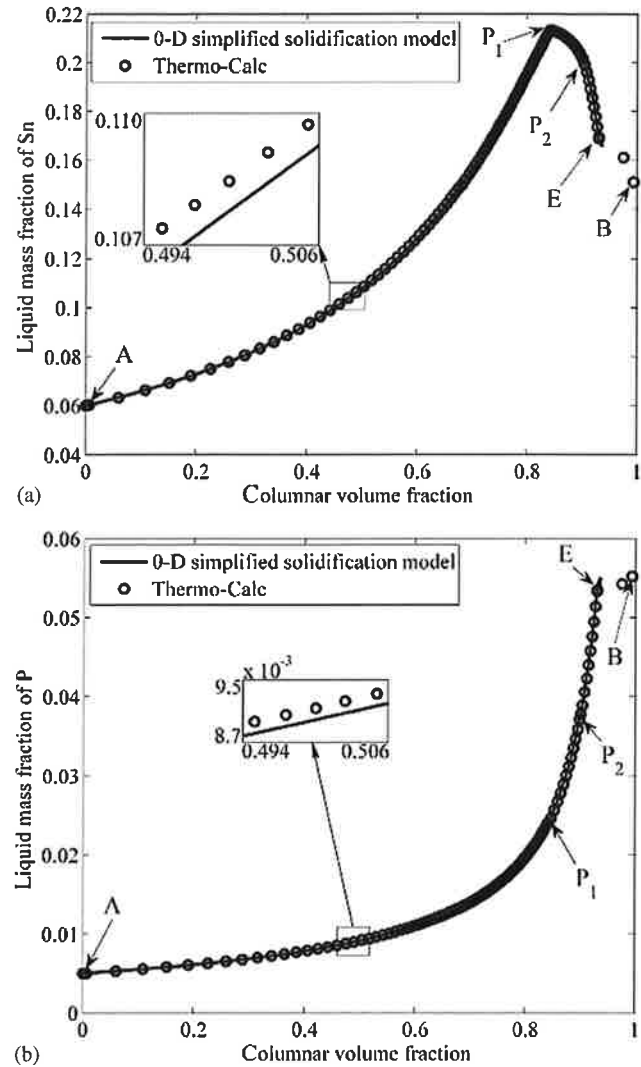
Fig. 3. Scheil curves calculated for the alloy CuSn6P0.05 for (a) Sn and (b) P with the 0-D solidification model (black line) and compared with a Thermo-Calc−Scheil calculation (circles). Here (A) is the initial alloy concentration, (P$_1$) corresponds to the beginning of the first peritectic reaction L + α → β, (P$_2$) to the beginning of the second peritectic reaction L + β → γ, (E) to the beginning of the eutectic groove, and (B) to the end of solidification according to the Thermo-Calc−Scheil model.

Further cooling leads to the formation of γ phase after reaching the second peritectic groove (P$_2$, Figs. 3 and 4) according to the peritectic reaction L + β → γ. The remaining melt starts to solidify in the eutectic groove of γ phase and Cu$_3$P (E, Figs. 3 and 4). From here the solidification path follows the eutectic groove further on to the eutectic groove of β and Cu$_3$P. According to Thermo-Calc−Scheil calculations, solidification ends here (Fig. 3a and b, B). The very last melt is, according to the Scheil model, expected to solidify with the ternary eutectic concentration of 15 wt.% Sn and 5.5 wt.% P. However, the calculation with the Thermo-Calc−Scheil model (Fig. 3a and b, B) stops before the ternary eutectic point due to the low remaining liquid volume fraction.

Principally, all three functions T_L (Eq. (13)), $\tilde{c}_c^{Sn}$ (Eq. (14)), and $\tilde{c}_c^{P}$ (Eq. (15)) can be approximated using their pointwise Thermo-Calc tabulations. Generally, any suitable interpolation can be applied. For the following upscaling of the model to industrial dimensions the three ther-
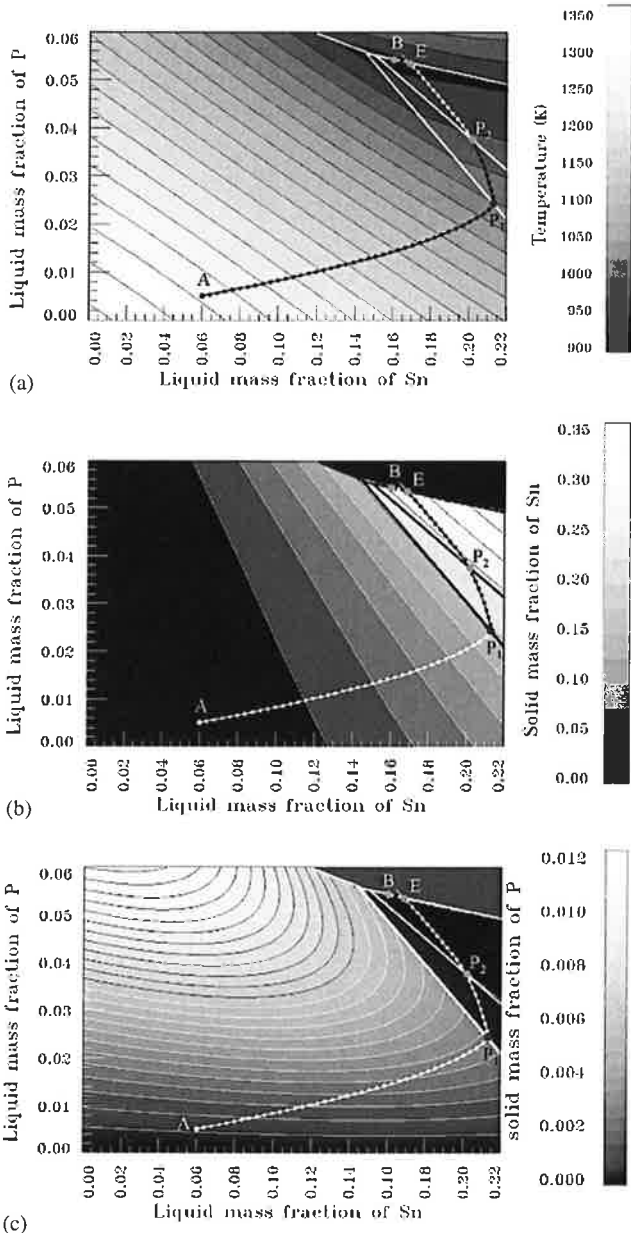
(a)

(b)

(c)

Fig. 4. Contour plots of (a) the liquidus temperature $T_L = T_L(\tilde{c}_l^{Sn}, \tilde{c}_l^P)$, (b) of the concentration of of Sn in solid, $\tilde{c}_c^{Sn} = \tilde{c}_c^{Sn}(\tilde{c}_l^{Sn}, \tilde{c}_l^P)$, (c) of the concentration of P in solid, $\tilde{c}_c^P = \tilde{c}_c^P(\tilde{c}_l^{Sn}, \tilde{c}_l^{P_c})$. Here (A) is the initial alloy concentration, (P$_1$) corresponds to the beginning of the first peritectic reaction $L + \alpha \rightarrow \beta$, (P$_2$) to the beginning of the second peritectic reaction $L + \alpha \rightarrow \gamma$, (E) to the beginning of the eutectic groove, and (B) to the end of solidification according to the Thermo-Calc–Scheil model.

modynamic functions Eqs. (17)–(19) were linearized around the initial composition (point A, Fig. 4).

3.2. Application to continuous casting of bronze

The binary two phase model as developed during the last few years [4–6] combined with the ternary thermodynamics information as described in this paper is applied to solidification simulation in a vertical continuous casting of bronze (CuSn6P0.5) to predict macrosegregation of Sn and P.

For the simulation a 2D axisymmetric geometry, as described in [7, 20] (Fig. 5), was used. The simulation considers

forced convection (inlet jet) and shrinkage flow, which is caused by different constant densities for the columnar and the liquid phase. Based on former studies [20, 23–25] feeding flow contributes significantly to the macrosegregation distribution occurring under these specific process conditions. Therefore, as a first approach, other flow phenomena such as thermo-solutal convection are ignored in these results. Material properties used are given in [20]. In the solidification simulation presented a permeability value of $\overline{K}_0 = 1.4 \times 10^{-5}$ was applied according to [20]. As boundary and initial conditions, the inlet temperature was considered to be $T_{inlet} = 1398$ K and the initial temperature $T_{init} = 1300$ K. The casting velocity $u_{cast} = 1.92$ mm s^{-1} was taken for the initial velocity of the melt. The initial casting temperature was set to $T_{cast} = 1398$ K, which is about 100 K above the liquidus temperature T_L of the initial alloy composition.

In the following, the results of this ternary simulation are discussed based on flow and thermodynamic parameters gained from the ternary calculation after having reached a steady state. Figure 5 shows the temperature field T_l of the strand in the continuous casting mold, Fig. 6 the columnar volume fraction f_c, Fig. 7a the liquid concentration for P, c_l^P, and Fig. 7b the liquid concentration for Sn, c_l^{Sn}. In Fig. 8 the melt velocity field is displayed (a) as arrows, and (b) as magnitude u_l. For the characterization of macrosegregation the so-called mixture concentration is used:

$$c_{mix}^{P,Sn} = \frac{c_l^{P,Sn}\rho_l f_l + c_c^{P,Sn}\rho_c f_c}{\rho_l f_l + \rho_c f_c} \qquad (21)$$

Figure 9 shows the macrosegregation pattern c_{mix} for both alloying elements P (a) and Sn (b). Here the highest and the lowest values displayed correspond to deviations of $\pm 10\%$ from the initial alloy composition. Above the columnar volume fraction $f_c = 0.83$, the results are meaningless, since the linearized thermodynamic functions do not take into account the phase changes (P$_1$, P$_2$ in Figs. 3 and 4) and therefore have to be ignored. The three isolines displayed in every contour plot correspond to (①) $T_L = 1295.5$ K, (②) $f_c = 0.5$ and (③) $f_c = 0.83$.
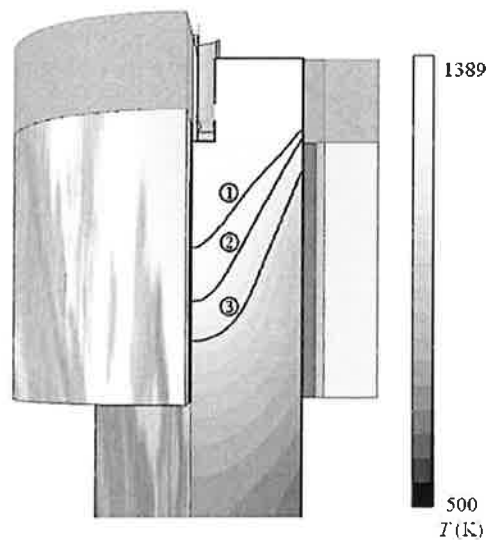

Fig. 5. Simulated temperature distribution in the continuous casting round strand for the ternary alloy CuSn6P0.5 in a case where feeding and inlet flow are considered. Black lines: (①) $T_L = 1295.5$ K, (②) $f_c = 0.5$ and (③) $f_c = 0.83$.

622

A. Ishmurzin et al.: Multiphase/multicomponent modeling of solidification processes
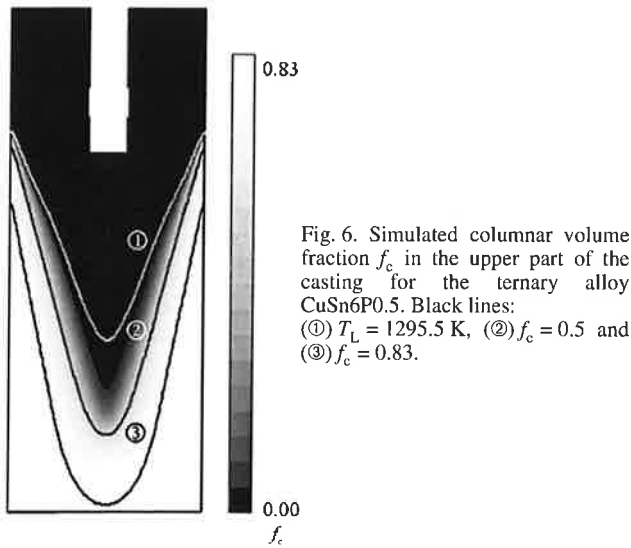

Fig. 6. Simulated columnar volume fraction f_c in the upper part of the casting for the ternary alloy CuSn6P0.5. Black lines: (①) $T_L = 1295.5$ K, (②) $f_c = 0.5$ and (③) $f_c = 0.83$.
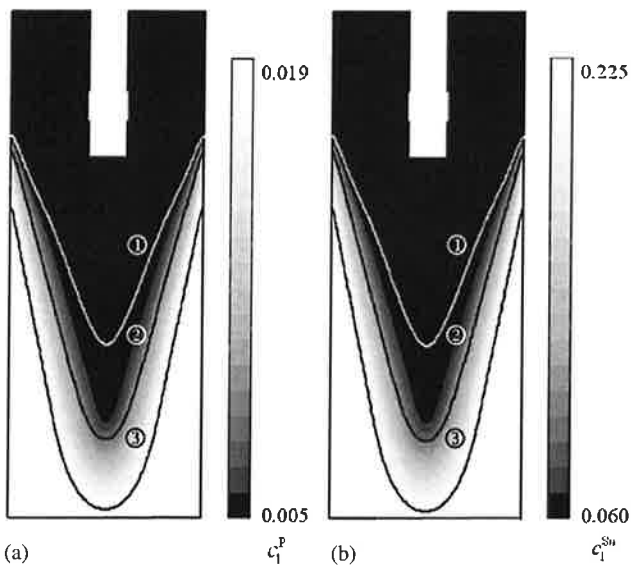

Fig. 7. Simulated mass fractions of P, c_l^P (a), and Sn, c_l^{Sn} (b) in the bulk melt in the upper part of the casting for the ternary alloy CuSn6P0.5. Black lines: (①) $T_L = 1295.5$ K, (②) $f_c = 0.5$ and (③) $f_c = 0.83$.

Columnar volume fraction f_c (Fig. 6) and liquid concentration of c_l^P and c_l^{Sn} (Fig. 7a and b) show that solidification starts at T_L and that the columnar volume fraction is $f_c = 0.83$ when the first peritectic groove is reached at about $c_l^{Sn} = 0.225$ mass fraction of Sn and $c_l^P = 0.019$ mass fraction of P. The simulated concentration of P, c_l^P, is lower than the one predicted by Thermo-Calc, which proposes a value of $c_l^P = 0.025$ mass fraction of P when the first peritectic groove is reached. This difference is due to linearization of thermodynamic functions (Eqs. (17)–(19)). Due to the fact that the phase transformation $L + \alpha \to \beta$ was not taken into account, the results show the volume fraction distribution just for the α phase.

The inlet jet causes the development of a big vortex with relatively high velocity in the upper region of the mold (I, Fig. 8). In addition, there is a second high velocity region occurring deep in the mushy zone (II, Fig. 8) due to feeding flow. The strand moves with casting velocity (III, Fig. 8) after columnar volume fraction exceeds $f_c = 0.83$. In these
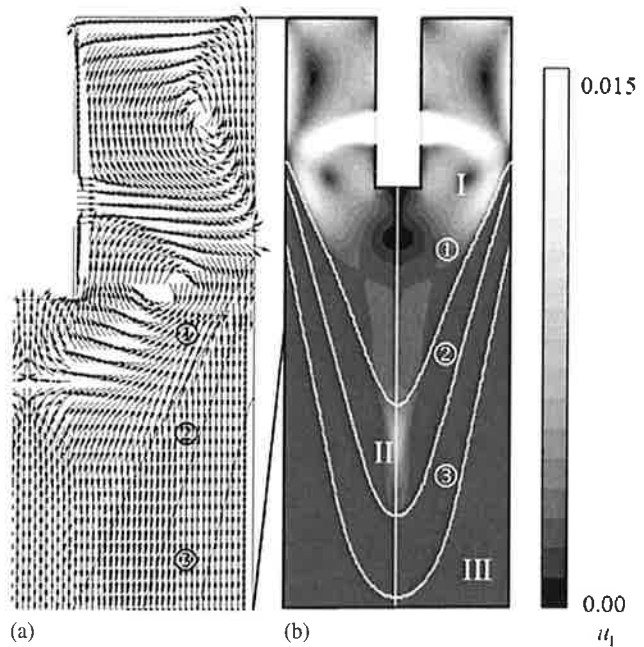

Fig. 8. Velocity field in the melt in the upper part of the casting for the ternary alloy CuSn6P0.5. Part (a) shows the vector field $\vec{u}_l$ in the region near the inlet, part (b) the velocity magnitude u_l. (I) indicates the position of the inlet vortex, (II) the second high velocity region in the center of the casting, and (III) the solidified strand moving with casting velocity $u_{cast} = 1.92$ mm s^{-1}. Black lines: (①) $T_L = 1295.5$ K, (②) $f_c = 0.5$ and (③) $f_c = 0.83$.
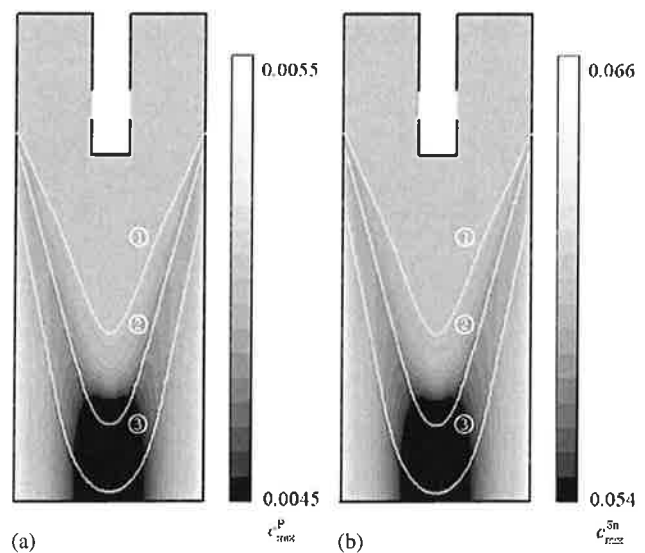

Fig. 9. Steady state distribution of the mixture concentration (a) c_{mix}^P and (b) c_{mix}^{Sn} in the upper part of the casting. Feeding flow causes positive macrosegregation near the wall and negative macrosegregation in the center of the casting. Black lines: (①) $T_L = 1295.5$ K, (②) $f_c = 0.5$ and (③) $f_c = 0.83$.

regions the applied drag force (described in [7]) causes entrapment of the remaining liquid between the dendrite network. Therefore the columnar phase and liquid phase move with the same casting velocity.

In the case presented, the main mechanism for macrosegregation is relative motion between melt and dendrites [7, 23–25]. As shown in Fig. 9a and b, macrosegregations at the surface of the strand for both elements, c_{mix}^P and c_{mix}^{Sn},

turned out to be positive and the macrosegregations in the center negative. Feeding flow is always directed from the dendrite tip towards its roots and thus carries segregated melt into the mush. Since the early work of Flemings [23–25], this phenomenon has been known to produce the so-called inverse segregation, positive macrosegregation, as discussed in solidification of binary alloys [20].

At the center of the cylindrical casting dendrite, tips approach each other and form a closing ring while solidification proceeds. At the same time, a relatively large mush volume in the center is solidifying and thus a lot of melt is needed to feed the corresponding shrinkage. This feeding flow causes the melt to be sucked into the solidifying mush through the solidifying 'ring of dendrites' and a strong relative downward motion of liquid occurs in this region (II, Fig. 8). This is why the mushy zone is fed with less- or non-segregated melt from the melt pool and negative macrosegregations occur in the central region of the casting.

The magnitude of the predicted macrosegregation for Sn and P is qualitatively almost the same. This can be explained by the fact, that for both alloying elements the same diffusion coefficients in the liquid $D_l^{Sn} = D_l^P$ were considered, since exact and reliable values are not known. In addition, both alloying elements are enriched almost linearly during solidification because of the observed linear solidification path in the α region.

4. Conclusions

A method to couple the solidification kinetics and thermodynamics in a multiphase Eulerian solidification model was presented. Thermodynamic data is suggested to be included into solidification simulation with the software FLUENT by using the tabulation and interpolation technique ISAT (In-Situ Adaptive Tabulation) [21].

In order to evaluate this idea, a 0-D solidification simulation was performed (considering no flow, no shrinkage). Comparisons between 0-D calculation and the Thermo-Calc–Scheil model results were done. Observations included:

- The predicted solidification path for the CuSn6P0.5 alloy is almost identical to the one predicted by the Thermo-Calc–Scheil model until the eutectic groove is reached. Further development is required to take the eutectic reaction into account.
- The $c_l^{P,Sn} - f_c$ curves of both 0-D simulation and Thermo-Calc–Scheil model are in good agreement. Some deviations are observed due to the difference between the solidification model presented, which is based on diffusion-controlled solidification kinetics, and Scheil's model, which assumes infinite diffusion in the liquid.

Additionally, a simulation of a CuSn6P0.5 round strand casting has been performed. Feeding flow and forced convection were taken into account. The main conclusions were:

- The predicted macrosegregation of Sn and P shows the same distribution pattern as observed in practice, namely positive at the wall and negative in the center of the strand.
- The predicted macrosegregation for Sn and P is qualitatively almost the same, which is not fully coincident

with observations in industry. Correct and reliable diffusion coefficients are required for reliable macrosegregation predictions.

Although the proposed model offers the possibility of coupling ternary thermodynamics with CFD, the lack of important material properties, such as diffusion coefficients in liquid and solid phases, constricts the prediction accuracy for as-cast processes.

Reference

[1] C. Beckermann, R. Viskanta: Appl. Mech. Rev. 46 (1993) 1–27.
[2] C. Beckermann: JOM. 49 (1997) 13–17.
[3] J. Ni, C. Beckerman: Metall. Trans. B 22 (1991) 349–361.
[4] A. Ludwig, M. Wu: Metall. Mater. Trans. A 33 (2002) 3673–3683.
[5] A. Ludwig, M. Wu: Mater. Sci. Eng. A 413–414 (2005) 109–114.
[6] M. Wu, A. Ludwig: Metall. Mater. Trans. A 37 (2006) 1613–1631.
[7] A. Ludwig, M. Gruber-Pretzler, M. Wu, A. Kuhn, J. Riedle: Fluid Dynamics and Materials Processing 1 (2006) 285–300.
[8] M. Wu, A. Ludwig: Metall. Mater. Trans. A 38 (2007) 1465–1475.
[9] P.D. Lee, A. Chirazi, R.C. Atwood, W. Wang: Mater. Sci. Eng. A 365 (2004) 57–65.
[10] M.C. Schneider, C. Beckermann: Metall. Mater. Trans. A 26 (1995) 2373–2388.
[11] M.C. Schneider, C. Beckermann: Int. J. Heat Mass Transfer 38 (1995) 3455–3473.
[12] J.O. Andersson, T. Helander, L. Höglund, P. Shi, B. Sundman: Calphad 26 (2002) 273–312.
[13] B. Sundman, B. Jansson, J.O. Andersson: Calphad 9 (1985) 153–190.
[14] T. Kraft, M. Rettenmayr, H.E. Exner: Prog. Mater. Sci. 42 (1997) 277–286.
[15] W.Q. Jie, R. Zhang, Z. He: Mater. Sci. Eng. A 413–414 (2005) 497–503.
[16] D. Larouche: Computer Coupling of Phase Diagrams and Thermochemistry 31 (2007) 490–504.
[17] H. Combeau, J.M. Drezet, A. Mo, M. Rappaz: Metall. Mater. Trans. A 27 (1996) 2314–2327.
[18] X. Dure, H. Combeau, M. Rappaz: Acta Mater. 48 (2000) 3951–3962.
[19] L. Thuinet, H. Combeau: J. Mater. Sci. 39 (2004) 7213–7219.
[20] A. Ludwig, M. Gruber-Pretzler, F. Mayer, A. Ishmurzin, M. Wu: Mater. Sci. Eng. A 413–414 (2005) 485–489.
[21] A. Ludwig, A. Ishmurzin, M. Gruber-Pretzler, F. Mayer, M. Wu, R. Tanzer, W. Schützenhöfer, in: H. Jones (Ed.), 5th Decennial International Conference on Solidification Processing, July 23–25, 2007, Sheffield, Tj International Ltd., Padstow (2007) 493–496.
[22] S.B. Pope: Combust. Theory Modelling 1 (1997) 41–63.
[23] M.C. Flemings, G.E. Nero: Trans. Metall. Society AIME 239 (1967) 1449–1461.
[24] M.C. Flemings, R. Mehrabien, G.E. Nero: Trans. Metall. Society AIME 242 (1967) 41–49.
[25] M.C. Flemings, G.E. Nero: Trans. Metall. Society AIME 242 (1967) 50–55.
[26] F. Mayer, M. Gruber-Pretzler, L. Könözsy, M. Wu, A. Ludwig, in: 2nd International Conference of Simulation and Modelling of Metallurgical Processes in Steelmaking Proceedings, (2007) 265–270

Bibliography

Correspondence address

Mr. Anton Ishmurzin
CD-Laboratory for Multiphase Modelling of Metallurgical Processes,
Department of Metallurgy, University of Leoben
A-8700 Leoben, Austria
Tel.: +43 3842 402 2225
Fax: +43 3842 402 2202
E-Mail: anton.ishmurzin@mu-leoben.at

You will find the article and additional material by entering the document number MK101682 on our website at www.ijmr.de